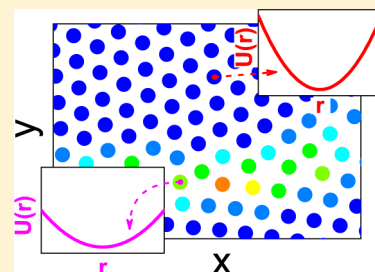


# Direct Imaging of Vibrations in Colloidal Crystals: In Equilibrium and in a Steady Drift

Erez Janai,<sup>†</sup> Alexander V. Butenko,<sup>†</sup> Andrew B. Schofield,<sup>‡</sup> and Eli Sloutskin<sup>\*,†</sup><sup>†</sup>Physics Department and Institute of Nanotechnology and Advanced Materials, Bar-Ilan University, Ramat-Gan 5290002, Israel<sup>‡</sup>The School of Physics and Astronomy, University of Edinburgh, Edinburgh EH9 3FD, U.K.**S** Supporting Information

**ABSTRACT:** Crystals of colloids, micron-size particles in a solvent, typically contain high concentrations of structural defects, limiting their applicability in self-assembly of metamaterials. Defects and grain boundaries play an important role for most properties of these crystals. Most previous research of colloidal crystals, by experiment and theory, focused on spatially averaged vibrational spectra: the differences in local environment between the bulk crystal particles and those at a grain boundary were typically neglected. We employ direct confocal microscopy and recent more accurate particle tracking algorithms to study the potential wells of individual particles in thermally vibrating quasi-two-dimensional colloidal crystals. We demonstrate that the energy landscape probed by a particle sensitively depends on its local environment. Furthermore, we emphasize the commonly neglected role of slight out-of-equilibrium drift of colloidal crystals, demonstrating that particle vibrations depend significantly on the drift velocity, so that the drifting crystals are softer, allowing an effective “drift temperature” to be defined.

**INTRODUCTION**

Crowded colloids of a low polydispersity,<sup>1</sup> thermalized in a molecular solvent by Brownian motion, minimize their free energy by crystal formation.<sup>2</sup> Colloidal crystals occur in natural sediments and may possibly play an important role in biomedicine, where ordered arrays of virus particles spontaneously self-assemble inside an infected cell.<sup>3</sup> Colloidal crystals are widely studied as potential self-assembled templates for photonic band gap materials, promising a wide range of future photonics applications.<sup>4,5</sup> Recently, colloidal crystals have also been employed in nanosphere lithography.<sup>6</sup>

Colloidal dynamics is overdamped by the viscous drag of the suspending medium, contrasting with the dynamics in simple atomic solids. Yet, colloidal physics mimics many important aspects of the collective phenomena occurring in atomic and molecular systems. Moreover, with the relevant time and length scales in colloidal systems being much longer than with atoms and molecules,<sup>7</sup> very detailed experimental information on colloids can be collected in real motion and with a single particle resolution, employing direct optical microscopy.<sup>8–14</sup> In particular, intense studies of vibration spectra in colloidal crystals have been recently carried out,<sup>15–21</sup> aiming at the fundamental understanding of the elastic properties of solid matter and the development of a common conceptual framework for crystal, glass, and granular matter.<sup>8,19,22</sup>

Most colloidal crystals are polycrystalline,<sup>23</sup> composed of small grains, and have relatively high concentrations of defects and grain boundaries (GBs).<sup>9,20</sup> This fact limits the applicability of colloidal crystals in photonics<sup>26</sup> and challenges the distinction between colloidal crystals and glasses.<sup>22</sup> Moreover, localized vibrations develop at defect locations,<sup>9,20</sup> reminiscent of dynamic and elastic heterogeneities in glass matter.<sup>24,25</sup>

Thus, the scattering techniques,<sup>15–17,21</sup> limited to probe only the spatial average of the lattice vibration dynamics, provide an incomplete information for colloidal crystals, where spatial inhomogeneity is non-negligible. Moreover, in many of the optical microscopy studies of colloidal crystal vibrations the focus is on the density of states of the vibration modes, with less attention being devoted to the actual real-space motion of the particles. Almost without exceptions,<sup>9,12,13</sup> these studies employ the displacement covariance analysis (DCA).<sup>8,10,11,18–20</sup> The DCA approach is based on the harmonic approximation of the interparticle potentials, which may not be valid for the colloids.<sup>15</sup> Furthermore, due to the complexity of the DCA, it is prone to numerical artifacts.<sup>27,28</sup> The influence of common experimental issues, such as minor sample drifts, sliding of GBs, and relaxation of metastable states is currently under investigation.<sup>20,28</sup> As a result, the potential wells of individual particles in colloidal crystals are still not fully characterized. In particular, the relation between the shape of the potential well and the local structure is not yet established.

To overcome these limitations of the previous studies, we carry out real space microscopy studies, correlating the local structure about each particle with its dynamics. In particular, we image by direct video-rate confocal microscopy the thermal motion of (many thousands of) individual colloidal spheres, forming a quasi-two-dimensional crystalline lattice (see raw confocal image in Figure 1). The distribution of displacements of a particle, with respect to its equilibrium position, allows the shape of its potential well to be characterized. We demonstrate

Received: February 28, 2016

Revised: March 24, 2016

Published: March 28, 2016

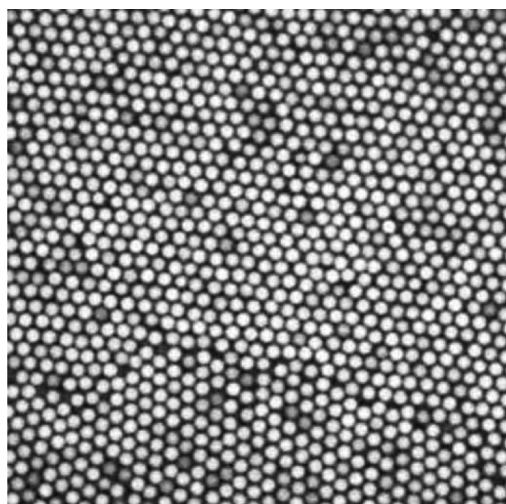


**Figure 1.** A raw confocal microscopy image of a polycrystalline colloidal lattice. Note the relatively large crystalline grains, separated by a clear grain boundary. The field of view is  $85 \times 85 \mu\text{m}$ .

that the potential well depends on the local environment of the particle within the solid; in particular, the wells next to defects and GBs are appreciably shallower. Furthermore, we demonstrate that particle vibrations are significantly modified in the presence of even a minor drift of the crystal through the solution, emphasizing the nontrivial role played by structural heterogeneities in these crystals.<sup>14,18,28</sup>

## ■ EXPERIMENTAL SECTION

To form a colloidal crystal, we suspend PMMA (poly(methyl methacrylate)) spheres, fluorescently labeled by Nile Red dye for confocal imaging, in dodecane ( $\text{CH}_3(\text{CH}_2)_{10}\text{CH}_3$ , Sigma-Aldrich,  $\leq 99\%$ ); the particle volume fraction is  $\sim 3\%$ . The particles are sterically stabilized by a poly-12-hydroxystearic acid (PHSA) monolayer, minimizing the van der Waals attractions,<sup>18,22</sup> so that the interparticle interactions are dominated by hard repulsions.<sup>29</sup> The synthesis of these particles and their properties are described in the literature,<sup>18,22,29–31</sup> the synthesis of PHSA and its properties are described in the literature<sup>30</sup> as well. We determine the diameter of our particles by dynamic and static light scattering as  $\sigma = 2.4 \mu\text{m}$ ; the size polydispersity of our particles is  $\leq 4\%$ . The colloidal suspension is loaded into a rectangular Vitrocom capillary ( $0.1 \times 2 \times 50 \text{ mm}$ ) and sealed with epoxy glue. The density mismatch between PMMA and dodecane is  $\Delta\rho \approx 0.3 \text{ g/cm}^3$ , so that the particles rapidly sediment, forming a crystalline bilayer at the bottom of the sample. In equilibrium conditions, this system is fully dominated by the gravity. In particular, the equilibrium sedimentation length<sup>32</sup>  $\delta_0 = k_B T / \Delta\rho v_p g$ , where  $v_p = \pi\sigma^3/6$  is the particle volume and  $g = 9.8 \text{ m/s}^2$ , is much smaller than  $\sigma$ , so that the thermal excitations are insufficient for a particle to leave the horizontal plane. To coat the capillary by PHSA adsorption, we add a small concentration ( $\sim 4\%$  w/w) of PHSA to the suspension, so that particle sticking to the capillary walls can be eliminated without changing significantly the colloid pair potentials.<sup>33</sup> Where complete coverage by PHSA has been achieved, even a tiny tilt of the sample led to a measurable drift of the crystalline layer, driven by the tiny sample-parallel component of the ambient gravity. Drift velocities were varied from 0.2 to 12 nm/s by accurately tuning the tilt angle of the sample; for that purpose,

the sample was mounted on a special tilt stage, allowing a resolution of  $0.05^\circ$ . Where any drift of the crystals was to be avoided, we employed samples with an incomplete PHSA coverage. In these samples, while particles in the microscope-illuminated area were free to vibrate, enough particles were stuck to the capillary bottom outside of the illuminated area, so that any drift of the crystals was blocked.

To image our colloids, we employ the Nikon A1R confocal laser scanning microscope in the resonant scanning mode, with an oil-immersed  $100\times$  Plan Apo objective. To achieve sufficient statistics, the  $512 \times 512$  frames are collected for about 30 min, with a digital resolution of  $0.17 \mu\text{m}/\text{pix}$  at  $\sim 4 \text{ fps}$ . We detect the center positions  $(x,y)$  of the particles within the bottom two-dimensional (2D) layer of our bilayer crystal, employing a modified version of the PLuTARC image-analysis algorithm,<sup>34</sup> based on the algorithm of Crocker and Grier.<sup>35</sup> An iterative algorithm is employed<sup>36</sup> to minimize the effect of the finite pixel size on the accuracy of particle localization. The accuracy of this algorithm in 2D has been previously estimated<sup>36</sup> as  $\sim 4 \text{ nm}$ , allowing small particle displacements to be accurately measured. The area fraction  $\eta$  of the particles in the sample is obtained directly from their number density  $n$ :  $\eta = n\pi\sigma^2/4$ . Finally, to follow the displacement of our particles between the subsequent frames, we track the particles by proximity.<sup>35</sup> The fact that all samples dealt with in the current work are crystalline simplifies particle tracking; still, the tracked trajectories were visually examined, to confirm their validity. While particles next to the boundary of the illuminated area move occasionally out of the frame and could not be tracked, a typical experiment yields full 30-min-long trajectories for more than  $10^3$  particles. After tracking, particle positions have been dedrifted by subtracting the average displacement of all particles; thus, the rest of the analysis is based only on particle displacements with respect to the center of mass (CM) of the sample.

## ■ RESULTS AND DISCUSSION

**Crystal Vibrations in Thermodynamic Equilibrium.** In the presence of GBs and defects, the structural order is imperfect, varying across the sample. To quantify the local crystallinity around a given particle, we employ the 6-fold symmetric orientational bond order parameter<sup>37,40</sup>  $\psi_6 = Z^{-1} \sum_i \text{Re}\{\exp(6i\Delta\theta_i)\}$ ; here the summation is carried out over the bonds to all  $Z$  nearest neighbors (NNs) of the particle and the angle  $\Delta\theta_i$  of the  $i$ -th bond is measured in a frame oriented with one of the NN bonds, chosen on random. A particle surrounded by  $Z = 6$  NNs in a perfectly hexagonal arrangement has  $\psi_6 = 1$ . Decreased  $\psi_6$  values are detected near static structural defects.<sup>9,40</sup> In addition, the instantaneous values of  $\psi_6$  are also reduced by thermal crystal vibrations, so that even the “perfect” experimental crystals typically have  $\psi_6 < 0.98$ .

To map the structural heterogeneity in our quasi-2D crystals,<sup>38</sup> we employ the time-averaged  $\langle\psi_6\rangle$  of all particles. Distinct individual grains are observed to be separated by low- $\psi_6$  boundaries [Figure 2(a)]. On first sight, quite surprisingly, the average bond lengths in the bulk of the crystalline grains seem longer than the ones at the boundaries [Figure 2(b)]. It may seem that this observation contrasts with the paradigm of liquid-like GBs having a lower density compared to the adjacent crystals.<sup>39</sup> However, while glassy boundaries, such as between the three-dimensional (3D) crystalline grains in systems of soft colloids,<sup>40</sup> can possibly be denser than the crystals, in quasi-two-dimensional crystals a different scenario takes place. In

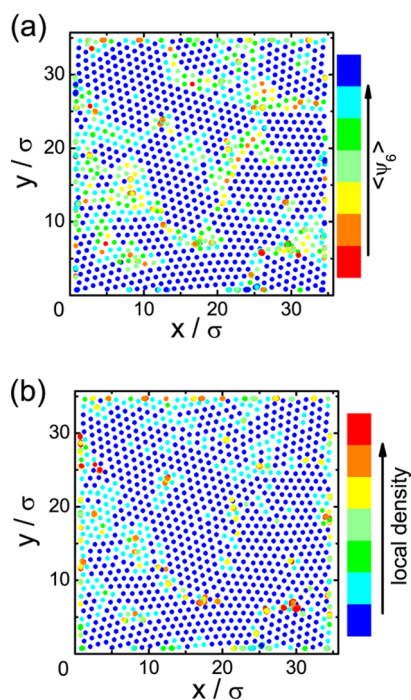


**Figure 2.** (a) The time-averaged particle positions in the quasi-two-dimensional colloidal crystal. The color of each particle indicates its average local bond-orientational order parameter  $\langle\psi_6\rangle$ . Note the significant structural heterogeneity, with the crystal grains separated by disordered grain boundaries (GBs). (b) The same crystal, with the color indicating the local in-plane density of particle centers. The increased density (shown in green) at the GBs is due to the increased fluctuations of plane-normal particle positions outside of the crystalline grains. By exploiting the freedom in the (plane-normal)  $z$  direction, the  $(x,y)$  coordinates of adjacent particles get closer than the particle diameter  $\sigma$ .

these quasi-2D crystals, a significant disorder in plane-normal  $z$ -coordinates of the particles at the GBs leads to a decreased in-plane separation between the particle centers: particles capable to move in the  $z$ -direction can have their  $x,y$ -coordinates closer together. We confirmed this mechanism by a full 3D confocal reconstruction of the sample, where the  $z$ -coordinates of the particles at the GBs are observed to be disordered and the average  $z$  is larger, compared to its value within the adjacent crystalline grains. The motion of GB particles along  $z$  makes the particle tracking more challenging: with the currently employed high-quality 2D-imaging of particle positions (Figure 1) limiting our image acquisition rate, we ultimately lose track of a particle, once it leaves the focal  $xy$  plane. In Figure 2, particles tracked in different time periods are overlaid. Thus, the GBs, where the motion along  $z$  is significant, appear more crowded; importantly this artificial crowding has no effect on instantaneous particle separations and  $\psi_6$  values, the averages of which are indicated by colors in Figure 2(a,b).

To test the impact of the crystals' structural heterogeneity on particle dynamics, we track the trajectories of all particles. In nondrifting samples, such as in Figure 2, all trajectories correspond to vibrations of particles about their average lattice positions. For our range of particle area fractions  $\eta$  and interparticle potentials, the distribution of particle displacements  $r$  is rotationally symmetric within the available statistics. The radial average  $P(r)$  of the distribution decays with  $r$ , indicating that the energetic penalty for large displacements is significant. If the effective potential wells probed by the

particles are harmonic, as commonly assumed,<sup>28</sup> we anticipate that  $P(r) \propto \exp\left(-\frac{1}{2}\kappa r^2\right)$ , where  $\kappa$  is the harmonic constant in units of  $k_B T/\sigma^2$ . However, colloidal crystals exhibit a significant structural heterogeneity (Figure 2), implying that  $\kappa$  values change across the sample. Spatially averaged  $P(r)$  includes  $\exp\left(-\frac{1}{2}\kappa r^2\right)$  contributions with different  $\kappa$ , so that  $\log(P(r))$  dramatically deviates from a linear dependence on  $r^2$ . The true local  $P(r)$  must be in a much better agreement with the harmonic approximation. To demonstrate this fact, we bin the  $P(r)$  data by the  $\langle\psi_6\rangle$  values of the vibrating particles. Thus, only particles in regions of similar crystallinity are averaged together,<sup>22</sup> so that the heterogeneity of  $\kappa$  in each of such  $P(r)$  averages is reduced. The resulting  $P(r)$ , for a range of different  $\langle\psi_6\rangle$  values, are shown in Figure 3(a), plotted as a function of  $r^2$

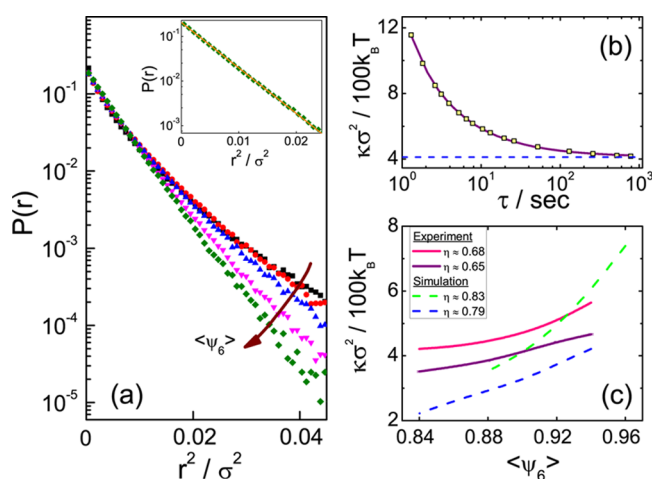


**Figure 3.** (a) The probability  $P(r)$  for a particle displacement in a crystal is plotted on a semilogarithmic scale, as a function of  $r^2$ . On this scale, a linear scaling would correspond to the effective potential well being perfectly harmonic. The data are binned by particles' crystallinity  $\langle\psi_6\rangle$  (see curved arrow). The data for  $\langle\psi_6\rangle = 0.95$  are zoomed-in in the inset, demonstrating the harmonic regime. The error bars are omitted for clarity, with even the largest statistical uncertainties (in the bottom right angle of the plot) reaching only  $\sim 30\%$ , of the same size as as the point scatter within each of the data sets (see Supporting Information). (b) The dependence of the apparent harmonic constant on the time span  $\tau$  of the trajectory (scatter) is fitted by  $\kappa(\tau) = C_1(\tau/\Delta t - 1)^{C_2} + \kappa(\tau \rightarrow \infty)$  (purple line), where  $\Delta t \approx 0.26$  s is the time interval between frames,  $C_1 > 0$  and  $C_2 < 0$  are arbitrary constants, and the true harmonic constant (dashes) is obtained in the long- $\tau$  limit. (c) Both in experiments (solid lines) and in MC simulations (dashes), the harmonic constant increases with the local crystallinity  $\langle\psi_6\rangle$ . For a given  $\langle\psi_6\rangle$ , a higher  $\kappa$  occurs in a denser sample (see legend). The slope of the simulated data is higher than in the experiments, suggesting that the GBs in the experimental samples may have a nonlocal effect on the elastic properties of the samples. The experimental statistical errors are only slightly larger than the line width.

on a semilogarithmic scale. As expected, spots characterized by a more perfect crystallinity correspond to a higher  $\kappa$ , as evidenced by the slopes in Figure 3(a). Notably, on the right-hand side of this plot, the data obtained for  $\langle\psi_6\rangle = 0.82$  and  $\langle\psi_6\rangle = 0.95$  differ by more than 1 order of magnitude, indicating that the local environment has a dramatic impact on thermal particle vibrations (see also Supporting Information). The plots are nearly linear, supporting the harmonic approximation; the linearity is further emphasized by the

inset, where  $r^2$  scale is smaller and the crystallinity is high. Importantly, as shown in Figure 2(b), the  $\langle\psi_6\rangle$  values exhibit a complex spatial distribution. Therefore, binning the  $P(r)$  of all particles by their spatial proximity (instead of the currently used  $\langle\psi_6\rangle$ -binning) would not lead to a similar agreement with the harmonic approximation. Remarkably, for a given range of  $r$ , the deviations of  $P(r)$  from the harmonic approximation are the smallest for particles located in the high-crystallinity regions [green diamonds in Figure 3(a)], suggesting that the appealing mean-field concept of a particle in an effective potential well loses its meaning for the highly disordered spots of the sample, where the effective potential is itself changing on a similar time scale.

For an accurate determination of the local  $\kappa$ , the trajectory of each particle should be sufficiently long, allowing all accessible regions of the potential well to be probed. When the trajectory is too short, some regions of the well are not probed, so that in these regions  $P(r) = 0$ . Thus, finite trajectories overestimate the value of  $\kappa$ , as shown in Figure 3(b), where  $\tau$  is the time span of a trajectory. The limiting values  $\kappa(\tau \rightarrow \infty)$  corresponding to the true thermodynamic  $\kappa$ , are shown in Figure 3(c). While the increase of  $\kappa$  with  $\langle\psi_6\rangle$  and  $\eta$  is not surprising, our Monte Carlo (MC) simulations of perfect crystals of hard disks (see Supporting Information) yield a higher  $\psi_6$ -slope for a similar  $\kappa$  (cf. green dashed simulated curve in Figure 3(c) to the experimental data sets). While Coulomb forces may increase the effective radius of the particles, leading to an increased effective  $\eta$  in the simulations (see legend), such inflation of the particles<sup>42</sup> is still unable to explain the discrepancy between theory and simulations observed in Figure 3(c). We speculate that the stronger  $\kappa$  ( $\langle\psi_6\rangle$ ) dependence in simulations is due to the absence of GBs in the simulated samples.<sup>41</sup>

**Vibrations in Drifting Crystals.** To test for a possible nonlocal effect of the grain boundaries, we increase the average grain size in our samples. For that to be achieved, the capillary is fully coated with the PHSA, so that particle immobilization at the bottom of the capillary is fully eliminated. As our crystals are formed by particle sedimentation from bulk suspension, any immobilized particles at the bottom of the sample severely limit structural relaxation during crystal growth, leading to a reduced size of the crystalline domains. However, with the immobilized particles completely eliminated, the crystals drift under very small tilts of the sample-containing capillary. Fine-tuning of the tilt angle (see Experimental Section) allows the drift velocity  $v_d$  to be adjusted, with the amplitude of the nonequilibrium contributions to the dynamics determined by  $v_d$ . Remarkably, while the interparticle potentials in our system are purely repulsive,<sup>15,34,42</sup> all particles belonging to a given crystalline grain drift together, so that the shear is mostly concentrated at the GBs. With the drift velocities of the individual grains being slightly different, the grains are not at rest in the reference frame coflowing with the CM of the polycrystalline sample; thus, dedrifting does not bring the effective potential wells of the particles to rest. Grain motion in the CM-frame is complex and may involve rotation (Figure 4(a)), challenging the quantitative analysis of  $P(r)$ . In particular, the distribution of particle displacements with respect to the average (dedrifted) particle positions is no longer symmetric under rotation. The distribution is stretched in a certain direction in the  $xy$  plane, leading to a similar apparent stretching of the potential wells probed by the particles. Clearly, such stretching of  $P(r)$  would lead to an incorrect  $\kappa$ , if not taken appropriately into account. The apparent potential wells of the different particles stretch, in

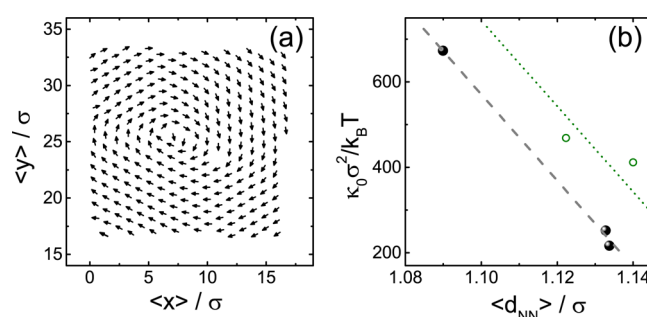


**Figure 4.** (a) Particle positions, averaged over a time scale far exceeding that of the particle vibrations, are shown to rotate with respect to the CM of the sample. The observed rotation is due to the velocities of the individual grains in a polycrystalline sample being unequal, with the shear concentrated at the GBs. (b) The extrapolated zero-drift harmonic constant  $\kappa_0$  (solid symbols), for  $\langle\psi_6\rangle = 0.9$ , decreases with the lattice constant ( $\langle d_{NN} \rangle$ ). The harmonic constants for the nondrifting samples, where the abundance of grain boundaries is higher (see Figure 3), are shown in open symbols. The lines are guides to the eye. The statistical y-errors are of the same size as the circles used to plot the data; the statistical x-error is  $\sim 0.5\%$ .

general, in different directions; see for example Figure 4(a), where the arrows indicate the stretching directions of the individual potential wells. The motion of grains with respect to the CM-frame is very slow, so that on the experimentally relevant time scale, each potential well is only stretched along a certain axis. Thus, the apparent equipotentials assume a shape of a rectangle capped by semicircles (the so-called, “Bunimovich stadium” potential).

To resolve  $\kappa$  for such a potential, we split the trajectory of each particle into time intervals of length  $\tau$ . For each value of  $\tau$ , the average  $P(r)$  is calculated. Then, we fit the  $P(r)$  for each  $\tau$  by

$$A \exp\left(-\frac{1}{2}\kappa(\tau)r^2\right) I_0\left[-\frac{1}{2}\kappa(\tau)r^2\right]^B$$

where  $A$  and  $B$  are free parameters and  $I_0$  is the modified Bessel function of the first kind. This choice is motivated by the radially averaged distribution in a well infinitely stretched along the  $x$  axis, being

$$P(r) = (2\pi)^{-1} \int_0^{2\pi} \exp\left(-\frac{1}{2}\kappa(\tau)y^2\right) d\theta \\ \propto \exp\left(-\frac{1}{4}\kappa r^2\right) I_0\left(-\frac{1}{4}\kappa r^2\right)$$

which for a finite stretching of a well should be combined with the expression used with a static well. To the second order in  $r$ , the logarithm of our fitting function scales as  $-1/2\kappa r^2$ , allowing  $\kappa(\tau \rightarrow \infty)$  to be identified with the conventional harmonic constant in a nondrifting crystal. We test our approach by fitting a simulated  $P(r)$  of a particle moving in a slowly drifting harmonic well. The fitting expression allows the correct  $\kappa$  of the well to be reproduced, indicating that the distortion of the potential well due to the drift is taken correctly into account; incorrect  $\kappa$  values are obtained when this drift-related correction is neglected. Thus, our approach accounts correctly for the imperfect dedrifting of particle positions resulted by the different drift velocities of the individual grains in a polycrystalline sample. We note in passing, that the same approach may be

beneficial for other fields where tracking of an individual nano- or colloidal particles in drifting wells is employed.<sup>43</sup>

The drift of crystalline domains through the suspending medium, while increasing the complexity of the  $P(r)$  analysis, results also into the emergence of complex out-of-equilibrium phenomena, which may possibly have a nontrivial effect on crystal vibrations. To test for a possible influence of such phenomena on  $\kappa$ , we measure  $P(r)$  for a range of different average drift velocities  $v_d$ . Strikingly,  $v_d$  as low as  $\sim 2.5$  nm/s is sufficient for  $\kappa$  to drop by about a factor of 2 for a given  $\langle\psi_6\rangle$  [see Figure 5(a,b)]. This drop in  $\kappa$ , indicating that the

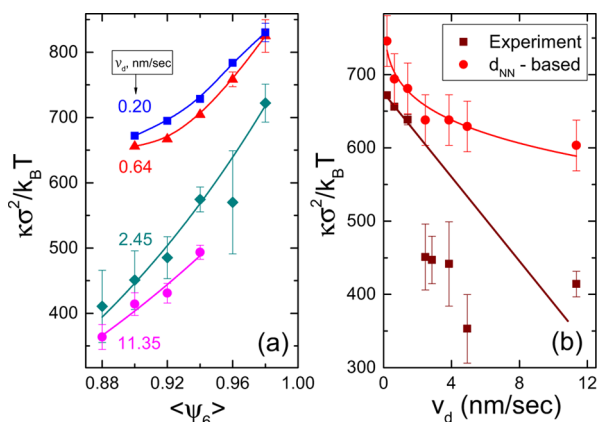


**Figure 5.** (a) For all drift velocities, the harmonic constant  $\kappa$  increases with the crystallinity ( $\langle\psi_6\rangle$ ), yet decreases with the drift velocity  $v_d$  (see labels). The statistical error bars are omitted where they are smaller than the symbol size. The accuracy of  $v_d$  determination is 1% for the lowest  $v_d$ , yet the accuracy improves by orders of magnitude for the larger  $v_d$ ; therefore, the corresponding error bars are not shown. (b) For a constant  $\langle\psi_6\rangle = 0.9$ , the experimental  $\kappa$  (brown squares) is a decreasing function of  $v_d$ . This softening of drifting crystals is both due to the increase of their lattice constant  $d_{NN}$  and due to the drift-induced fluctuations increasing their effective temperature. The effect of  $d_{NN}$  variation with  $v_d$  is demonstrated in pink circles, representing the variation of  $\kappa$  with  $d_{NN}(v_d)$  in an absence of drift-induced fluctuations [see Figure 4(b)].

amplitude of particle vibrations grows with the drift, has two contributions: (a) a slight increase of the lattice constant with the drift; (b) energy fluctuations associated with the drift. To decouple these contributions, we extrapolate the data for different samples to  $v_d = 0$ . The corresponding harmonic constants  $\kappa_0$  scale with  $d_{NN}$  [solid symbols in Figure 4(b)], extrapolating to zero at  $\eta \approx 0.68$ , slightly lower than the melting of a hard-disk hexatic phase.<sup>44</sup> We employ this  $\kappa_0(d_{NN})$  scaling and the measured  $d_{NN}(v_d)$  to predict the  $\kappa(v_d)$  variation in an absence of drift-associated energy fluctuations. The resulting  $\kappa(v_d)$  [pink circles in Figure 5(b)] significantly overestimate the experimental values (brown squares), indicating that much of the drift-induced softening of the crystals can be attributed directly to the energy fluctuations, which are missing for the pink circles.

In settling of glass beads in 3D, the hydrodynamically induced spatial fluctuations of particle settling velocity have been demonstrated to thermalize the system, providing an effective temperature scale, called “the gravitational temperature for sedimentation”.<sup>45</sup> In our case, since  $\kappa$  is expressed in units of  $k_B T/\sigma^2$ , an increase of the effective “drift temperature” by a factor of  $\sim 1.4$ , compared to the common thermodynamic temperature, could justify the observed softening of the drifting

crystals, for  $v_d \approx 4$  nm/s. However, the effective thermalization mechanism is very different from that in the fluid 3D sediments: the settling velocities of our crystals are lower by orders of magnitude, the backflow of the solvent is negligible, and particles belonging to each crystalline domain drift together at roughly the same velocity. Importantly, while the Péclet number<sup>45</sup> ( $Pe$ ) of an individual PMMA sphere in dodecane, in the relevant range of substrate tilt angles, is of the order of 0.1, a much larger  $Pe \approx 10^5$  is associated with the motion of a typical crystalline grain, so that the non-Brownian effects may be very significant. In view of the increased motion of the GB particles along  $z$ , discussed above, we suggest that for a crystalline domain to drift faster by some  $\Delta v_d$  compared to its neighboring domains, it must occasionally push the particles at its GB up (along  $z$ ) by a significant fraction of  $\sigma$ ; with the GBs in our samples being curved and the interparticle potentials almost perfectly hard, any relative motion between the crystals would otherwise be prohibited by geometry. Thus, the nonequilibrium sedimentation length  $\delta_{neq}$  of the particles at the GBs must be of the order of  $\sigma/2$ . Expressing the effective thermal energy due to the drift by  $k_B T_{neq}$  we obtain  $k_B T_{neq} = \delta_{neq} \Delta \rho v_p g \approx \sigma \Delta \rho v_p g / 2$ , so that  $k_B T_{neq} \approx 3k_B T$ . A 2D crystal of  $N \approx 900$  particles has  $N_b \approx 100$  particles at its boundary. Assuming that the nonequilibrium energy fluctuations of  $\sim 3k_B T$  per GB particle are equally distributed throughout the crystal, each particle in the crystal gets an extra energy of  $\sim 0.3 k_B T$ , which may possibly account for the reduction of  $\kappa/k_B T$  by a factor of  $\sim 1.4$  (cf. brown squares and pink circles in Figure 5(b)). A direct measurement of particle dynamics along  $z$  at the GBs may allow, in the future, this somewhat speculative, hand-waving argument to be substantiated and the full  $\kappa(v_d)$  to be understood.

Finally, we note that the  $\kappa$  values shown in the solid symbols in Figure 4(b) are lower (for a given  $d_{NN}$ ), compared to Figure 3(c) [reproduced in open symbols in Figure 4(b)], where the crystalline grains were smaller. This observation suggests that the GBs, where much of the crystal dynamics is concentrated, may have an unexpected constraining effect on the adjacent high- $\langle\psi_6\rangle$  particles: the vibration amplitude of these particles is severely reduced, further emphasizing the complex outcomes of structural heterogeneities in these crystals.

## CONCLUSIONS

We have demonstrated by a real-space analysis of particle vibrations in a colloidal crystal that the amplitude of particle vibration is a sensitive function of the local crystallinity. In particular, we detect and quantify the decrease in this amplitude for higher values of the bond orientational crystalline order parameter. Employing a controlled drift of crystals on tilted substrates, we have demonstrated a drift-induced softening of crystal vibrations. Our experiments provide a wealth of local information on particle vibrations, complementing the commonly used displacement covariance analysis. Future experimental and theoretical studies should allow a direct connection to be developed between these two different approaches, en route to a deeper understanding of vibration modes in ordered and disordered solids.

## ASSOCIATED CONTENT

### Supporting Information

The Supporting Information is available free of charge on the ACS Publications website at DOI: 10.1021/acs.jpcc.6b02070.

Details of the computer simulation procedures and of the drift measurements (PDF)

## AUTHOR INFORMATION

### Corresponding Author

\*E-mail: [eli.sloutskin@biu.ac.il](mailto:eli.sloutskin@biu.ac.il). Phone: +972 (3) 738 4506.

### Notes

The authors declare no competing financial interest.

## ACKNOWLEDGMENTS

The authors thank P. J. Lu for sharing his PLuTARC codes and Y. Rabin for the fruitful discussions. This research was supported by the Israel Science Foundation (no. 85/10, no. 1668/10). Some of the equipment was funded by the Kahn Foundation. A.B.S. is partially funded by the UK Engineering and Physical Sciences Research Council grant EP/J007404/1.

## REFERENCES

- (1) Phan, S.-E.; Russel, W. B.; Zhu, J.; Chaikin, P. M. Effects of polydispersity on hard sphere crystals. *J. Chem. Phys.* **1998**, *108*, 9789–9795.
- (2) Bishop, K. J. M.; Chevalier, N. R.; Grzybowski, B. A. When and why like-sized, oppositely charged particles assemble into diamond-like crystals. *J. Phys. Chem. Lett.* **2013**, *4*, 1507–1511.
- (3) Hull, R. *Plant Virology*, 5th ed.; Elsevier: New York, 2014.
- (4) Waterhouse, G. I. N.; Chen, W. T.; Chan, A.; Jin, H.; Sun-Waterhouse, D.; Cowie, B. C. C. Structural, optical, and catalytic support properties of  $\gamma$ -Al<sub>2</sub>O<sub>3</sub> inverse opals. *J. Phys. Chem. C* **2015**, *119*, 6647–6659.
- (5) Kim, S.-H.; Lee, S. Y.; Yang, S.-M.; Yi, G.-R. Self-assembled colloidal structures for photonics. *NPG Asia Mater.* **2011**, *3*, 25–33.
- (6) Colson, P.; Henrist, C.; Cloots, R. Nanosphere lithography: A powerful method for the controlled manufacturing of nanomaterials. *J. Nanomater.* **2013**, *2013*, 948510.
- (7) Song, X.; Zhang, M.; Wang, J.; Li, P.; Yu, J. Optimization design for DTB industrial crystallizer of potassium chloride. *Ind. Eng. Chem. Res.* **2010**, *49*, 10297–10302.
- (8) Kaya, D.; Green, N. L.; Maloney, C. E.; Islam, M. F. Normal modes and density of states of disordered colloidal solids. *Science* **2010**, *329*, 656–658.
- (9) Alsayed, A. M.; Islam, M. F.; Zhang, J.; Collings, P. J.; Yodh, A. G. Premelting at defects within bulk colloidal crystals. *Science* **2005**, *309*, 1207–1210.
- (10) Keim, P.; Maret, G.; Herz, U.; von Grünberg, H. H. Harmonic lattice behavior of two-dimensional colloidal crystals. *Phys. Rev. Lett.* **2004**, *92*, 215504.
- (11) Ghosh, A.; Mari, R.; Chikkadi, V. K.; Schall, P.; Maggs, A. C.; Bonn, D. Low-energy modes and Debye behavior in a colloidal crystal. *Phys. A* **2011**, *390*, 3061–3068.
- (12) Bongers, J.; Versmold, H. Microscopic investigations of the single particle dynamics in colloidal crystals. *J. Chem. Phys.* **1996**, *104*, 1519–1523.
- (13) Weiss, J. A.; Larsen, A. E.; Grier, D. G. Interactions, dynamics, and elasticity in charge-stabilized colloidal crystals. *J. Chem. Phys.* **1998**, *109*, 8659–8666.
- (14) Ueno, T.; Yamazaki, K.; Nishio, I. Hydrodynamic effects of particle motions in colloidal crystal. *AIP Conf. Proc.* **2006**, *832*, 287–290.
- (15) Cheng, Z.; Zhu, J.; Russel, W. B.; Chaikin, P. M. Phonons in an entropic crystal. *Phys. Rev. Lett.* **2000**, *85*, 1460–1463.
- (16) Penciu, R. S.; Krieger, H.; Petekidis, G.; Fytas, G.; Economou, E. N. Phonons in colloidal systems. *J. Chem. Phys.* **2003**, *118*, 5224–5240.
- (17) Megens, M.; Vos, W. L. Particle excursions in colloidal crystals. *Phys. Rev. Lett.* **2001**, *86*, 4855–4858.
- (18) Reinke, D.; Stark, H.; von Grünberg, H.-H.; Schofield, A. B.; Maret, G.; Gasser, U. Noncentral forces in crystals of charged colloids. *Phys. Rev. Lett.* **2007**, *98*, 038301.
- (19) Zargar, R.; Russo, J.; Schall, P.; Tanaka, H.; Bonn, D. Disorder and excess modes in hard-sphere colloidal systems. *Europhys. Lett.* **2014**, *108*, 38002.
- (20) Chen, K.; Still, T.; Schoenholz, S.; Aptowicz, K. B.; Schindler, M.; Maggs, A. C.; Liu, A. J.; Yodh, A. G. Phonons in two-dimensional soft colloidal crystals. *Phys. Rev. E* **2013**, *88*, 022315.
- (21) Tata, B. V. R.; Jena, S. S. Ordering, dynamics and phase transitions in charged colloids. *Solid State Commun.* **2006**, *139*, 562–580.
- (22) Tan, P.; Xu, N.; Schofield, A. B.; Xu, L. Understanding the low-frequency quasilocalized modes in disordered colloidal systems. *Phys. Rev. Lett.* **2012**, *108*, 095501.
- (23) Giuliani, M.; González-Viñas, W.; Poduska, K. M.; Yethiraj, A. Dynamics of crystal structure formation in spin-coated colloidal films. *J. Phys. Chem. Lett.* **2010**, *1*, 1481–1486.
- (24) Kawasaki, T.; Tanaka, H. Structural origin of dynamic heterogeneity in three-dimensional colloidal glass formers and its link to crystal nucleation. *J. Phys.: Condens. Matter* **2010**, *22*, 232102.
- (25) Mizuno, H.; Mossa, S.; Barrat, J.-L. Acoustic excitations and elastic heterogeneities in disordered solids. *Proc. Natl. Acad. Sci. U.S.A.* **2014**, *111*, 11949–11954.
- (26) Blanco, A.; Gallego-Gómez, F.; López, C. Nanoscale morphology of water in silica colloidal crystals. *J. Phys. Chem. Lett.* **2013**, *4*, 1136–1142.
- (27) Schindler, M.; Maggs, A. C. Truncated correlations in video microscopy of colloidal solids. *Soft Matter* **2012**, *8*, 3864–3874.
- (28) Henkes, S.; Brito, C.; Dauchot, O. Extracting vibrational modes from fluctuations: A pedagogical discussion. *Soft Matter* **2012**, *8*, 6092–6109.
- (29) Bryant, G.; Williams, S. R.; Qian, L.; Snook, I. K.; Perez, E.; Pincet, F. How hard is a colloidal ‘hard sphere’ interaction? *Phys. Rev. E: Stat. Phys., Plasmas, Fluids, Relat. Interdiscip. Top.* **2012**, *66*, 060501.
- (30) Antl, L.; Goodwin, J. W.; Hill, R. D.; Ottewill, R. H.; Owens, S. M.; Papworth, S.; Waters, J. A. The preparation of poly(methyl methacrylate) latices in non-aqueous media. *Colloids Surf.* **1986**, *17*, 67–78.
- (31) Liber, S. R.; Borohovich, S.; Butenko, A. V.; Schofield, A. B.; Sloutskin, E. Dense colloidal fluids form denser amorphous sediments. *Proc. Natl. Acad. Sci. U. S. A.* **2013**, *110*, 5769–5773.
- (32) Palacci, J.; Cottin-Bizonne, C.; Ybert, C.; Bocquet, L. Sedimentation and effective temperature of active colloidal suspensions. *Phys. Rev. Lett.* **2010**, *105*, 088304.
- (33) Roberts, G. S.; Sanchez, R.; Kemp, R.; Wood, T.; Bartlett, P. Electrostatic charging of nonpolar colloids by reverse micelles. *Langmuir* **2008**, *24*, 6530–6541.
- (34) Lu, P. J.; Shutman, M.; Sloutskin, E.; Butenko, A. V. Locating particles accurately in microscope images requires image-processing kernels to be rotationally-symmetric. *Opt. Express* **2013**, *21*, 30755–30763.
- (35) Crocker, J. C.; Grier, D. G. Methods of digital video microscopy for colloidal studies. *J. Colloid Interface Sci.* **1996**, *179*, 298–310.
- (36) Gao, Y.; Kilfoil, M. L. Accurate detection and complete tracking of large populations of features in three dimensions. *Opt. Express* **2009**, *17*, 4685–4704.
- (37) Murray, C. A.; Sprenger, W. O.; Wenk, R. A. Comparison of melting in three and two dimensions: Microscopy of colloidal spheres. *Phys. Rev. B: Condens. Matter Mater. Phys.* **1990**, *42*, 688–703.
- (38) Hersam, M. C. Defects at the two-dimensional limit. *J. Phys. Chem. Lett.* **2015**, *6*, 2738–2739.
- (39) Dash, J. G.; Fu, H.; Wettlaufer, J. S. The premelting of ice and its environmental consequences. *Rep. Prog. Phys.* **1995**, *58*, 115–167.
- (40) Nagamanasa, K. H.; Gokhale, S.; Ganapathy, R.; Sood, A. K. Confined glassy dynamics at grain boundaries in colloidal crystals. *Proc. Natl. Acad. Sci. U. S. A.* **2011**, *108*, 11323–11326.

(41) Schiøtz, J.; Di Tolla, F. D.; Jacobsen, K. W. Softening of nanocrystalline metals at very small grain sizes. *Nature* **1998**, *391*, 561–563.

(42) Cohen, A. P.; Janai, E.; Rapaport, D. C.; Schofield, A. B.; Sloutskin, E. Structure and interactions in fluids of prolate colloidal ellipsoids: Comparison between experiment, theory and simulation. *J. Chem. Phys.* **2012**, *137*, 184505.

(43) Lindner, M.; Nir, G.; Vivante, A.; Young, I. T.; Garini, Y. Dynamic analysis of a diffusing particle in a trapping potential. *Phys. Rev. E* **2013**, *87*, 022716.

(44) Bernard, E. P.; Krauth, W. Two-step melting in two dimensions: First-order liquid-hexatic transition. *Phys. Rev. Lett.* **2011**, *107*, 155704.

(45) Segrè, P. N.; Liu, F.; Umbanhowar, P.; Weitz, D. A. An effective gravitational temperature for sedimentation. *Nature* **2001**, *409*, 594–597.